



Towards Model-Based Characterization of Biomechanical Tumor Growth Phenotypes

Daniel Abler^{1,2} , Philippe Büchler² , and Russell C. Rockne¹ 

¹ City of Hope, Duarte, CA, USA
{dabler, rrockne}@coh.org

² University of Bern, Bern, Switzerland
{daniel.abler, philippe.buechler}@artorg.unibe.ch

Abstract. Gliomas are the most common malignant brain tumors in adults, with Glioblastoma (GBM) being the most aggressive subtype. GBM is clinically evaluated with magnetic resonance imaging (MRI) and presents with different growth phenotypes, involving varying degrees of healthy tissue invasion and tumor induced herniation, also known as mass effect. GBM growth in the brain is frequently modeled as a reaction-diffusion process in which varying ratios of diffusion and proliferation coefficients mimic the observed spectrum of growth phenotypes ranging from nodal to diffuse. However, reaction-diffusion models alone are insufficient to explain tumor-induced mass effect on normal peripheral tissues, which is a critical clinical issue.

We propose an analysis method and framework for estimating GBM growth properties (proliferation, invasiveness, displacive potential) from MRI data routinely collected in the clinical management of GBM. This framework accounts for the mass-effect of the growing tumor by assuming a coupling between local tumor-cell density and volumetric expansion of the tissue.

We evaluate the reconstruction workflow on synthetic data that represents a range of realistic growth situations and levels of uncertainty. For most parameter combinations (90%) that correspond to tumors detectable by T1-weighted MRI, target parameters are recovered with a relative error of less than 15%.

Keywords: Mechanically-coupled tumor growth · Inverse problem · Image-based modeling

1 Tumor Mass-Effect in Glioblastoma

Gliomas are the most frequent malignant brain tumors in adults, with Glioblastoma (GBM) being the most malignant subtype. The rapid invasive growth of this tumor frequently results in lesions that cause healthy-tissue deformation, midline shift or herniation. Biomechanical forces, such as those caused by the

growing tumor, are known to shape the tumor environment and contribute to tumor progression [6]. Additionally, in brain tumors, elevated solid stress is linked to neuronal loss and neurological dysfunction [10]. In GBM patients, increased tumor mass-effect has been shown to be associated to poor prognosis [11]. This suggests that the propensity of an individual tumor to displace healthy tissue can provide information about the tumor micro-environment and might be of predictive value for treatment and outcome. However, tumors of similar imaging volumes have been observed to give rise to different amounts of tumor mass-effect [11], Fig. 1, possibly resulting in distinct mechanical stress distributions and magnitudes.

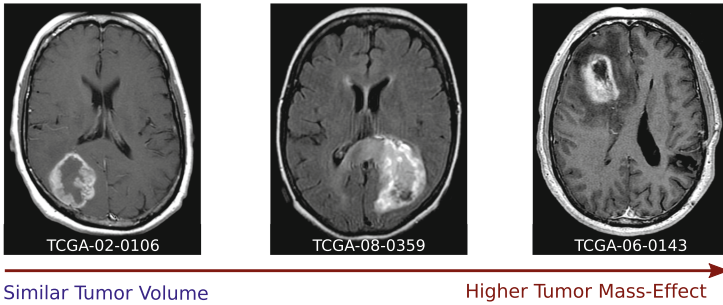


Fig. 1. Tumors of similar imaging volume can exhibit different degrees of mass-effect. Images from [TCGA-GBM](#).

The growth characteristics of GBM have been studied extensively using mathematical models that describe the invasive growth of this tumor as a reaction-diffusion process. These models characterize GBM growth phenotypes on a spectrum from mostly *nodular* to mostly *diffuse*, corresponding to *invasive* growth. However, it remains unknown whether differences in proliferative and invasive potential are sufficient to explain the observed differences in mass-effect.

To investigate the relation between *proliferation*, *invasiveness*, tumor mass-effect and its manifestation on clinical imaging, we are developing a framework for characterizing *mechanically-coupled* GBM growth. By finding solutions to the inverse growth problem, we aim to establish whether *proliferation* and *invasiveness* can explain the observed variability in tumor mass-effect, or whether distinct biomechanical growth phenotypes of GBM exist that differ also in their “*displaciveness*”.

Here, we present an approach for estimating parameters of a mathematical tumor growth model that accounts for the mass effect of the tumor. We propose a workflow for applying this approach to MR imaging data, and evaluate its accuracy and robustness in a parametric study on 2D synthetic data that represents a range of realistic growth situations and levels of uncertainty.

2 Materials and Methods

2.1 Mathematical Model of Mechanically-Coupled Tumor Growth

Mathematical models of tumor mass-effect were initially studied in the context of atlas-based image segmentation [7]. These models were soon extended to account for tumor growth dynamics by coupling to single-species reaction diffusion equations [3]. More recently, information about tumor induced mechanical-stresses has been incorporated in biophysical tumor growth models to inform local motility of tumor cells in the brain [5], and multi-species mechanically-coupled growth models have been developed [12].

Here we use a single-species mechanically-coupled reaction-diffusion model [1] that captures the dominant aspects of macroscopic GBM growth: the diffuse invasion of the growing tumor into surrounding healthy tissue, and the resulting mass effect.

Invasive growth is modeled phenomenologically as a reaction-diffusion process:

$$\frac{\partial c}{\partial t} = \nabla \cdot (D \nabla c) + \rho c (1 - c) c, \quad (1)$$

with normalized cancer cell density $c(\mathbf{x}, t)$ and diffusion coefficient $D = D(\mathbf{x})$. Tumor cell proliferation is assumed to follow logistic growth with proliferation rate $\rho = \rho(\mathbf{x})$.

To simulate the tissue-displacing mass-effect of the growing tumor, we model the growth domain as elastic continuum in which the actual deformation $\mathbf{u}(\mathbf{x}, t)$ of a tissue element is given by the combination of growth-induced strains $\hat{\boldsymbol{\epsilon}}^{\text{growth}}$ and strains caused by the elastic response of the tissue. We assume a linear constitutive relation between mechanical stress $\hat{\boldsymbol{\sigma}}$ and strain $\hat{\boldsymbol{\epsilon}}$, as well as mechanically isotropic materials that are fully characterized by Young's modulus E and Poisson ratio ν .

$$\hat{\boldsymbol{\sigma}}(\mathbf{u}) = \frac{E}{2(1+\nu)} \hat{\boldsymbol{\epsilon}}(\mathbf{u}) + \frac{E\nu}{(1+\nu)(1-2\nu)} \text{Tr} \hat{\boldsymbol{\epsilon}}(\mathbf{u}) \mathbf{1} \quad (2a)$$

$$\hat{\boldsymbol{\epsilon}}(\mathbf{u}) = \frac{1}{2} (\nabla \mathbf{u} + (\nabla \mathbf{u})^T) \quad (2b)$$

Additionally, we postulate a linear coupling between tumor cell density and growth-induced strain with isotropic coupling strength λ :

$$\hat{\boldsymbol{\epsilon}}^{\text{growth}}(c) = \lambda \mathbf{1} c. \quad (3)$$

Table 1 summarizes variables and parameters of this model.

The model is implemented using the *FEniCS* library¹ [2] for solving the model equations via the Finite Element Method. This implementation employs first and second order Lagrange elements for spatial interpolation of displacement $\mathbf{u}(\mathbf{x})$ and density $c(\mathbf{x})$ fields, respectively. Time-stepping is performed using a first order implicit numerical scheme.

¹ <https://fenicsproject.org>.

Table 1. Variables and parameters of the mathematical model.

Symbol	Parameter name	Units
$c(\mathbf{x}, t)$	tumor cell density	normalized to c_0
$\mathbf{u}(\mathbf{x}, t)$	tumor-induced displacements	mm
D	diffusion coefficient/diffusivity	mm^2/d
ρ	proliferation rate	1/d
λ	coupling constant	
E	young's modulus	kPa
ν	poisson's ratio	

2.2 Simulation Domain

Growth is simulated in a 2D computational domain Ω based on the *SRI24*² [8] atlas of normal human brain anatomy. The atlas contains tissue classes for White Matter (WM), Grey Matter (GM) and Cerebrospinal Fluid (CSF). The latter was divided into two compartments to distinguish fluid-filled brain ventricles from the remaining CSF, Fig. 2. Distinct isotropic growth and mechanical tissue parameters D_i , ρ_i , E_i , ν_i were assigned to each subdomain Ω_i .

The simulation domain was spatially discretized into a mesh of triangular elements with maximum cell diameter of 1.42 mm. We assumed the growth domain to be free of any initial mechanical stresses and approximate the displacement constraint imposed by the rigid skull by zero-displacement Dirichlet boundary conditions on the domain boundary. Similarly, tumor cells were prevented from leaving the domain by zero-flux von-Neumann boundary conditions. The tumor was initialized by a Gaussian-shaped 2D tumor cell density field $c_0 = c(\mathbf{x}_0, t = 0)$ centered at the seed location \mathbf{x}_0 and with standard-deviation of 1 mm.

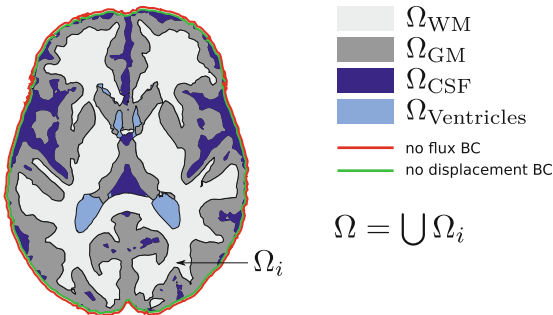


Fig. 2. Schema of brain simulation domain Ω with subdomains Ω_i for white matter (WM), grey matter (GM), surrounding cerebrospinal fluid (CSF) and CSF-filled ventricles.

² <https://www.nitrc.org/projects/sri24/>.

2.3 Estimation of Growth Parameters as Inverse Problem

Given the forward model, Eqs. (1) to (3), growth parameter identification can be framed as a PDE-constrained optimization problem with the aim to identify the set of parameters \mathbf{p}^{opt} that minimizes an objective functional J . Such a functional can be constructed by comparing the primary variables of the simulation, $c(\mathbf{x})$ and $\mathbf{u}(\mathbf{x})$ to corresponding target tumor cell density $c^*(\mathbf{x})$ and tissue displacement $\mathbf{u}^*(\mathbf{x})$ fields at a specific observation time point k .

$$J = \|c(\mathbf{x}, t_k) - c^*(\mathbf{x}, t_k)\|_2^2 + \|\mathbf{u}(\mathbf{x}, t_k) - \mathbf{u}^*(\mathbf{x}, t_k)\|_2^2 \quad (4)$$

Simulated tumor cell density $c(\mathbf{x}, t_k)$ and tissue deformation $\mathbf{u}(\mathbf{x}, t_k)$ fields at the corresponding simulation time step t_k are constrained by the forward model and depend on the current set of simulation parameters \mathbf{p} .

While medical imaging provides information about those quantities, detailed spatial maps are not directly observable. A commonly used approach in the GBM modeling literature estimates tumor cell density by associating specific imaging detection thresholds to different imaging modalities. Tumor features visible in T1- and T2-weighted MR-imaging have been linked to different levels of relative tumor cell density: $c > 0.80$ for visibility on T1-weighted contrast enhanced MRI, and $c > 0.16$ for visibility on T2-weighted (T2) MRI [14]. Routine clinical imaging for brain tumors thus provides two views of the unknown tumor cell density field $c^*(\mathbf{x})$, corresponding to two indicator functions $\chi_{T1}^*(\mathbf{x})$ and $\chi_{T2}^*(\mathbf{x})$ that identify the positions \mathbf{x} where $c(\mathbf{x}) \geq 0.80$ and $c(\mathbf{x}) \geq 0.16$, respectively. Tissue displacements in the brain can be estimated by deformable image registration between two imaging time points or relative to a healthy brain atlas, which allows an estimate for the tumor-induced displacement field $\tilde{\mathbf{u}}^*(\mathbf{x})$ to be obtained at diagnosis and between follow-up scans.

Given these target fields, an alternative objective function based on image-derivable target quantities can be formulated:

$$J = \|\chi_{T1}(\mathbf{x}, t_k) - \chi_{T1}^*(\mathbf{x}, t_k)\|_2^2 + \|\chi_{T2}(\mathbf{x}, t_k) - \chi_{T2}^*(\mathbf{x}, t_k)\|_2^2 + \|\mathbf{u}(\mathbf{x}, t_k) - \tilde{\mathbf{u}}^*(\mathbf{x}, t_k)\|_2^2 \quad (5)$$

with $\chi_i(\mathbf{x}, t_k)$ obtained by applying the respective detection threshold to the simulated density field $c(\mathbf{x}, t_k)$.

The adjoint method provides an efficient approach for computing the gradient $\frac{dJ}{d\mathbf{p}}$ and thus for solving the minimization problem $\min_{\mathbf{p}}(J)$. This implementation uses the *dolphin-adjoint* library³ for automatic derivation of the discrete adjoint equations for our forward model, Eqs. (1) to (3), and optimization functionals Eqs. (4) and (5), respectively.

2.4 Evaluation of Parameter Estimation Approach

We evaluated the performance of this parameter estimation approach in two different scenarios using synthetic data generated from simulation of the for-

³ <http://www.dolphin-adjoint.org>.

Table 2. Parameter ranges for parametric study. Growth parameters D_{WM} , ρ , λ were varied across physiological ranges (\min , \max) resulting in 100 parameter combinations. A fixed relation was assumed between diffusivity in GM and WM: $D_{\text{WM}} = 5 \cdot D_{\text{GM}}$ [13].

Parameter	min	max	step	# steps	init	Units
D_{WM}	0.05	0.20	0.05	4	0.001	mm^2/d
ρ	0.02	0.18	0.04	5	0.001	1/d
λ	0.02	0.18	0.04	5	0.001	

ward model. In both cases, the duration of tumor growth T , as well as initial conditions, tumor seed location and zero initial displacements, were assumed to be known. Mechanical tissue properties were fixed to $E_{\text{WM/GM}} = 3.00$ kPa, $E_{\text{CSF}} = 1.00$ kPa, $\nu_{\text{WM/GM}} = 0.45$, $\nu_{\text{CSF}} = 0.30$.

Reconstruction from Forward Simulation: First, we aimed to recover the simulation parameters of the forward model $\mathbf{p} = \{D_{\text{WM}}, D_{\text{GM}}, \rho_{\text{WM}}, \rho_{\text{GM}}, \lambda\}$, directly from results of the forward simulation, using density $c(\mathbf{x}, T)$ and displacement $\mathbf{u}(\mathbf{x}, T)$ fields from the final simulation time point T as reference, Eq. (4).

Reconstruction from Image-Derived Target Fields: Second, we studied a more realistic scenario in which we aimed to recover the simulation parameters from information available from routine clinical MR imaging, Eq. (5). This scenario accounts for the noise associated to the derivation of target fields χ_{T1}^* , χ_{T2}^* , \mathbf{u}^* from this information. In this setting, we characterized the performance of the proposed parameter estimation approach in a parametric study by sampling ($n = 100$) from realistic ranges of three independent growth parameters $\mathbf{p} = \{D_{\text{WM}}, \rho, \lambda\}$, Table 2.

For each parameter combination \mathbf{p} , tumor growth was simulated for a time period T with time steps $\Delta t = 1\text{d}$, Fig. 3(A). At the final simulation time point, density $c(\mathbf{x}, T)$ and displacement $\mathbf{u}(\mathbf{x}, T)$ fields were extracted and used to construct a synthetic dataset that mimics the kind of information that can be obtained from routine clinical MR imaging, Fig. (3)(B). The simulated density field $c(\mathbf{x}, T)$ was subjected to thresholds $c(\mathbf{x}) \geq 0.16$ and $c(\mathbf{x}) \geq 0.80$, resulting in two indicator functions corresponding to the portion of the tumor visible on T2-weighted and T1-weighted MRI. We used these indicator functions χ_{T1}^* , χ_{T2}^* as target fields in the optimization process, Eq. (5). The simulated displacement field $\mathbf{u}(\mathbf{x}, T)$ was used to deform the anatomical (T1 MRI) atlas on which growth had been simulated. From the resulting images we estimated the tumor-induced displacement by deformable image registration, using the symmetric image normalization method (SyN) as implemented in the *Advanced Normalization Tools* (ANTs)⁴. This reconstructed displacement field $\tilde{\mathbf{u}}^*$ served as target field in the optimization process, Fig. (3)(C).

⁴ <https://github.com/ANTsX/ANTs>.

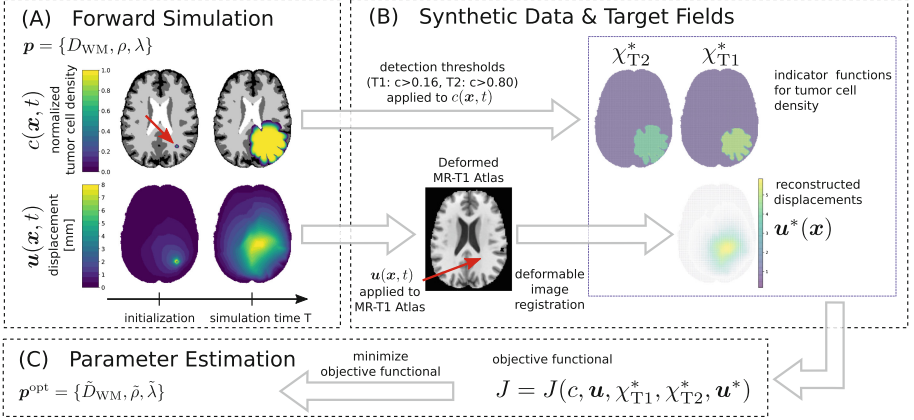


Fig. 3. Workflow of parametric study: Results from forward simulation (A) were used to create synthetic target fields (B) to which the proposed parameter estimation approach (C) was applied to recover the original simulation parameters $\mathbf{p}^{opt} \approx \mathbf{p}$.

We applied this approach to each synthetic data set to obtain a set of *reconstructed* growth parameters $\mathbf{p}^{opt} = \{\tilde{D}_{WM}, \tilde{\rho}, \tilde{\lambda}\}$. Parameter optimization was initialized with the values indicated in column *init* in Table 2. Duration of tumor growth T and initial conditions were assumed to be known in each optimization scenario.

We compared reconstructed \mathbf{p}^{opt} to actual \mathbf{p} growth parameters in terms of their absolute value and relative reconstruction error $\epsilon_i = (p_i^{opt} - p_i)/p_i$.

3 Results

3.1 Forward Simulation

Tumor evolution and tumor-induced mass-effect were simulated for $T = 250$ d days forward in time starting from an initial Gaussian-shaped tumor cell distribution. Figure 4 illustrates the evolution of tumor cell density $c(\mathbf{x}, T)$ and the resulting tumor-induced displacement field $\mathbf{u}(\mathbf{x}, T)$. Compression of the lateral ventricles by the growing tumor is evident from the last row of Fig. 4.

3.2 Reconstruction from Forward Simulation

Forward simulation over $T = 250$ d was repeated for seed positions in three different locations, indicated by red arrows in Fig. 5: in GM (*Case 1*), WM (*Case 2*), and at the interface between GM and WM (*Case 3*). Using density and displacement fields from the final time point, $c^*(\mathbf{x}, T)$, $\mathbf{u}^*(\mathbf{x}, T)$, we tried to recover the simulation parameters of the forward model by PDE-constrained optimization.

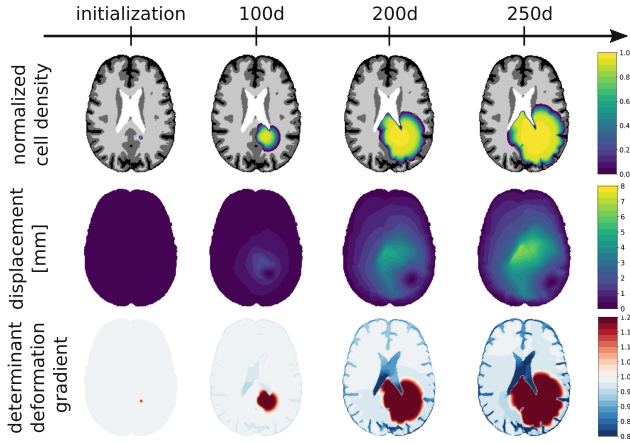


Fig. 4. Simulated evolution of tumor growth and mass effect.

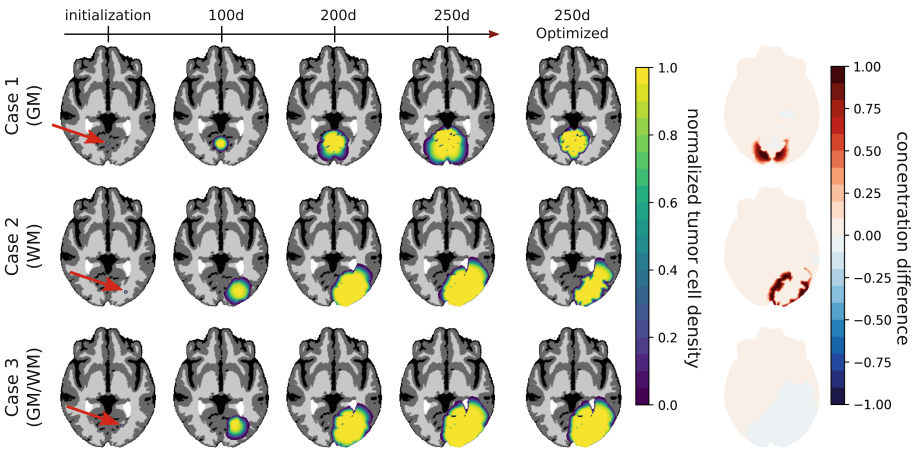


Fig. 5. Simulated evolution of tumor growth from seeds in three different locations: GM (*Case 1*), WM (*Case 2*), and at the interface between GM and WM (*Case 3*). Simulated density fields based on the reference parameters \mathbf{p}^{ref} are compared ($T = 250\text{d}$) to density fields based on the parametersets obtained from optimization (\mathbf{p}^{opt1} , \mathbf{p}^{opt2} , \mathbf{p}^{opt3} , see Table 3). Note that GBM very rarely grow or migrate into the cerebellum. The seed locations have been chosen to illustrate the parameter estimation approach on approximately equally sized contiguous patches of GM and WM. (Color figure online)

Table 3 summarizes reference parameters for the forward simulation \mathbf{p}^{ref} , their initialization for optimization \mathbf{p}^{init} and optimization results \mathbf{p}^{opt} for the three scenarios depicted in Fig. 5.

Reference growth parameters could be recovered correctly for the brain region most affected by the tumor: GM properties for *Case 1* and WM properties for *Case 2*. For *Case 3*, which grew with substantial involvement of both WM and GM domains, target parameters for both regions were recovered correctly.

Table 3. Reference parameters for forward simulations and reconstructed parameters for cases 1 to 3 in Fig. 5.

	ρ_{WM} [1/d]	ρ_{GM} [1/d]	D_{WM} [mm ² /d]	D_{GM} [mm ² /d]	λ
Forward model reference \mathbf{p}^{ref}	0.08	0.080	0.100	0.020	0.150
Optimization initialization \mathbf{p}^{init}	0.010	0.010	0.010	0.010	0.200
Case 1 \mathbf{p}^{opt1}	0.010	0.080	0.010	0.020	0.150
Case 2 \mathbf{p}^{opt2}	0.080	0.010	0.100	0.010	0.150
Case 3 \mathbf{p}^{opt3}	0.080	0.080	0.100	0.020	0.150

3.3 Reconstruction from Image-Derived Target Fields

In a second evaluation, the workflow shown in Fig. 3 was applied to $n = 100$ combinations of growth parameters $\mathbf{p} = \{D_{\text{WM}}, \rho, \lambda\}$, Table 2, for a duration of $T = 100$ d in two different growth domains.

Figure 6 compares the resulting distribution of reconstructed parameter values to their target values. Distributions of reconstructed D_{WM} and ρ_{WM} are concentrated around the respective target values. Estimates corresponding to the highest parameter values explored in this study ($D_{\text{WM}} = 0.20$ mm²/d, $\rho_{\text{WM}} = 0.18$ d⁻¹) show the largest uncertainty with few outliers extending their distribution towards values below the target value. Most reconstructions of λ slightly overestimate the target value; parameter estimates for the lowest coupling ($\lambda = 0.02$) are associated with highest uncertainty and biased towards larger values.

Only tumors that are sufficiently large and dense to be detected on both T1 and T2 weighted MRI were included in Fig. 6. Slowly or diffusively growing tumors with high D/ρ ratios may not be visible in one or both MR modalities and therefore do not contribute to the objective functional, Eq. (5), resulting in higher relative reconstruction errors for this group of parameter combinations. Figure 7 shows the fraction of reconstructed parameter sets in function of the maximum relative reconstruction error in each parameter, and visibility of the tumor on

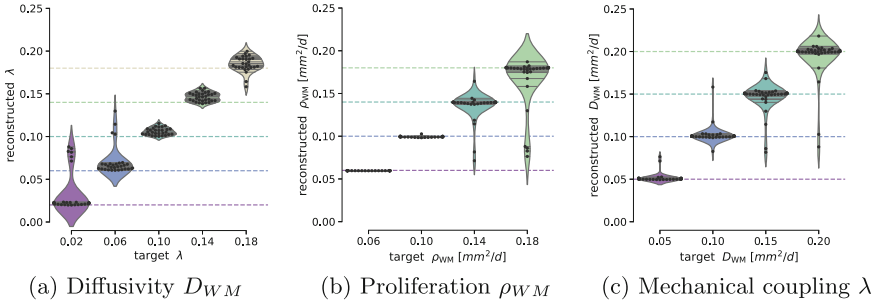


Fig. 6. Distribution of reconstructed parameter values versus target values. Horizontal lines indicate the target value used in the forward simulation. Only simulations with $c(\mathbf{x}, T)$ exceeding T1 and T2 detection thresholds are included; therefore, no reconstructed values are reported for simulation parameter $\rho = 0.02d^{-1}$ in (b).

T1- and T2-weighted MR imaging. Provided that the tumor is detectable in T1-weighted MRI, we obtained relative reconstruction errors of less than 15% for about 90% of all converged optimization cases (190 of 200) across the parameter space.

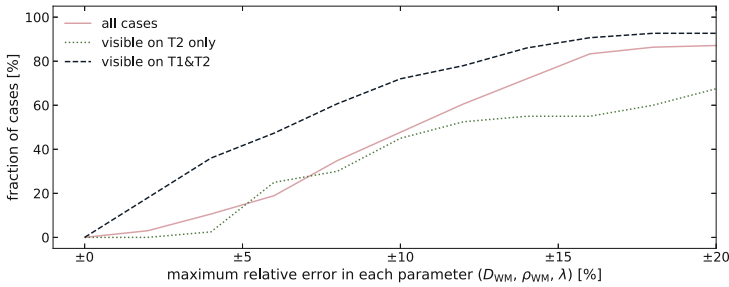


Fig. 7. Fraction of reconstructed parameter sets in function of the maximum relative reconstruction error. A value of $\pm\zeta$ on the x-axis indicates that all relative reconstruction errors ϵ_i simultaneously fulfill $|\epsilon_i| < |\zeta|$ for all parameters $i \in \{D_{WM}, \rho_{WM}, \lambda\}$.

4 Discussion

This study proposes an imaging biomarker for tumor mass-effect that can be derived from parametrizations of a biomechanically-coupled tumor growth model.

While adjoint-based optimization of parameters in a similar mechanically coupled tumor growth model had been explored before [4], the characterization of this approach was limited to 1D, and tumor-induced tissue deformation was

taken into account only at selected landmark positions. More recent advances include frameworks, such as [9] which combines adjoint parameter estimation of a reaction diffusion model with image registration, but does not explicitly model tumor mass-effect.

Here, we presented a method for estimating parameters of a mechanically coupled tumor growth model from routine clinical imaging information of glioma patients. Performance of this method was characterized on 2D synthetic data in a reconstruction workflow that mimics data and associated uncertainties of real reconstruction scenarios. We demonstrated self-consistency of this approach and found relative reconstruction errors of less than 15 % for about 90 % of cases, provided that the tumor is detectable in T1 weighted MRI.

This study assumed that origin and duration of tumor growth were known for the optimization process. However, and particularly when applied to a single observation at the time of diagnosis, tumor origin and duration of growth may be unknown. Preliminary tests indicate similar reconstruction performance when seeding the optimization process at the center-of-mass position of the observed synthetic tumor. Estimated values of the ratio D/ρ are expected to be independent of the growth period. However, the degree to which D/ρ and λ can be identified simultaneously under this condition remains to be studied.

We aim to use the developed framework to characterize GBM growth in terms of the tumor's invasiveness and its displacive potential. As next steps, we plan to characterize this approach in 3D and to investigate its application to patient MR images.

Acknowledgement. The research leading to these results has received funding from the European Union's Horizon 2020 research and innovation programme under the Marie Skłodowska-Curie grant agreement No. 753878.

References

1. Abler, D., Büchler, P.: Evaluation of a mechanically coupled reaction–diffusion model for macroscopic brain tumor growth. In: Gefen, A., Weihs, D. (eds.) *Computer Methods in Biomechanics and Biomedical Engineering*. LNB, pp. 57–64. Springer, Cham (2018). https://doi.org/10.1007/978-3-319-59764-5_7
2. Alnæs, M., et al.: The FEniCS Project Version 1.5. *Archive of Numerical Software*, vol. 3 (2015). <https://doi.org/10.11588/ans.2015.100.20553>
3. Clatz, O., et al.: Realistic simulation of the 3-D growth of brain tumors in MR images coupling diffusion with biomechanical deformation. *IEEE Trans. Med. Imaging* **24**(10), 1334–1346 (2005). <https://doi.org/10.1109/TMI.2005.857217>
4. Hogeia, C., Davatzikos, C., Biros, G.: An image-driven parameter estimation problem for a reaction-diffusion glioma growth model with mass effects. *J. Math. Biol.* **56**(6), 793–825 (2008). <https://doi.org/10.1007/s00285-007-0139-x>
5. Hormuth, D.A., Eldridge, S.L., Weis, J.A., Miga, M.I., Yankeelov, T.E.: Mechanically coupled reaction-diffusion model to predict glioma growth: methodological details. In: von Stechow, L. (ed.) *Cancer Systems Biology*. MMB, vol. 1711, pp. 225–241. Springer, New York (2018). https://doi.org/10.1007/978-1-4939-7493-1_11

6. Jain, R.K., Martin, J.D., Stylianopoulos, T.: The role of mechanical forces in tumor growth and therapy. *Ann. Rev. Biomed. Eng.* **16**(1), 321–346 (2014). <https://doi.org/10.1146/annurev-bioeng-071813-105259>
7. Mohamed, A., Davatzikos, C.: Finite element modeling of brain tumor mass-effect from 3D medical images. In: Duncan, J.S., Gerig, G. (eds.) *MICCAI 2005*. LNCS, vol. 3749, pp. 400–408. Springer, Heidelberg (2005). https://doi.org/10.1007/11566465_50
8. Rohlfing, T., Zahr, N.M., Sullivan, E.V., Pfefferbaum, A.: The SRI24 multichannel atlas of normal adult human brain structure. *Human Brain Mapping* **31**(5), 798–819 (2010). <https://doi.org/10.1002/hbm.20906>
9. Scheufele, K., Mang, A., Gholami, A., Davatzikos, C., Biros, G., Mehl, M.: Coupling brain-tumor biophysical models and diffeomorphic image registration. *Comput. Methods Appl. Mech. Eng.* **347**, 533–567 (2019)
10. Seano, G., et al.: Solid stress in brain tumours causes neuronal loss and neurological dysfunction and can be reversed by lithium. *Nature Biomed. Eng.*, January 2019. <https://doi.org/10.1038/s41551-018-0334-7>
11. Steed, T.C., et al.: Quantification of glioblastoma mass effect by lateral ventricle displacement. *Sci. Rep.* **8**(1), December 2018. <https://doi.org/10.1038/s41598-018-21147-w>
12. Subramanian, S., Gholami, A., Biros, G.: Simulation of glioblastoma growth using a 3d multispecies tumor model with mass effect. *J. Math. Biol.* **79**(3), 941–967 (2019). <https://doi.org/10.1007/s00285-019-01383-y>
13. Swanson, K.R., Alvord, E.C., Murray, J.D.: A quantitative model for differential motility of gliomas in grey and white matter. *Cell Prolif.* **33**(5), 317–329 (2000)
14. Swanson, K.R., Rostomily, R.C., Alvord, E.C.: A mathematical modelling tool for predicting survival of individual patients following resection of glioblastoma: a proof of principle. *Br. J. Cancer* **98**(1), 113–119 (2008)